Controlling asymmetric transmission in layered natural hyperbolic crystals

*Reed Jones**[a], Robert E. Camley[a], Rair Macêdo[b]*

[a]UCCS BioFrontiers Center and Department of Physics and Energy Science, University of Colorado, Colorado Springs, Colorado Springs, CO, USA;

[b]James Watt School of Engineering, Electronics & Nanoscale Engineering Division, University of Glasgow, Glasgow G12 8QQ, United Kingdom

*rjones12@uccs.edu

RECEIVED DATE (to be automatically inserted after your manuscript is accepted if required according to the journal that you are submitting your paper to)

We explore the electromagnetic properties of a structure composed of two optically active materials—each layer contains a hyperbolic crystal with its anisotropy axis rotated with respect to the crystal surface. Through this, we can control the transmission spectra where at one frequency, light with a positive incident angle is transmitted while it is absorbed for a negative incident angle and the reverse occurs at a second frequency. Using a Gaussian beam analysis, we determine in which material layer the absorption occurs. In a radiating line current source study, we obtain tunable output collimated beams. From these discoveries, our structure can be applied as an efficient frequency or angle selector, demultiplexer or filter.

KEYWORDS: polaritons, hyperbolic materials, asymmetry, transmission, collimated beams

1. Introduction

First observed in 1902,[1] a polariton is an interaction between light and matter, where the matter is excited by and coupled to a propagating electromagnetic wave.[2] Theoretical work on polaritons began in the 1950s[3–7] and since then they have been well studied in many different physical systems such as antiferromagnets,[8–10] metallic thin films,[11–13] gratings,[14–16] superlattices,[17–20] Bose-Einstein condensates,[21–23] optical transistors[24] and amplifiers.[25,26] Recently, polaritons have been studied in cavities,[27–29] topological insulators[30,31] and lasers[32–34] and are still at the forefront of technology as they are excellent candidates to open access to terahertz imaging and the next generation of wireless communication.[35]

A class of polaritons that has recently gained considerable interest is that of hyperbolic polaritons.[36–39] They have the hyperbolic name because their bulk dispersion relation looks like a hyperbola[40] and to obtain such behavior anisotropic materials are required. More specifically, hyperbolic dispersion requires that the sign on one of the diagonal components of the permeability or permittivity tensor is opposite from the others.[41–43] Crystal quartz is known to be a natural hyperbolic material and it has several regions of frequency—in the infrared band—where its ordinary and extraordinary permittivity tensor components have opposite signs due to active phonons.[44]

Recent work has shown that a rotation of the anisotropy direction with respect to a crystal surface can yield several unusual effects including asymmetric transmission patterns. In these single crystals, there are narrow ranges of frequencies where this asymmetry occurs.[45] Later work exploited the asymmetric transmission in quartz to enhance absorption patterns[44] and since then other nanostructures have also been created to elucidate the same effects.[46]

In this paper, we investigate the case of a multi-layered system, comprising two hyperbolic media layers (both crystal quartz), each with a different anisotropy direction with respect to the

surface. We find that by combining positive and negative rotations of the anisotropy axis, we gain more control in the location of the asymmetry in the transmission compared to what is possible with a single film. For example, we show that waves with a positive incident angle can be blocked at one frequency while waves with a negative incident angle are transmitted. By choosing a different frequency we find that negative incident angles can be blocked while positive incident angles are now transmitted. We explore how the asymmetry is correlated with different attenuations, depending on the inversion of the direction of propagation.

Furthermore, since the introduction of metamaterial super lenses, hyperbolic materials have been used as flat lenses which focus radiation from a point source--a phenomenon which can be modelled using an oscillating line current source placed above the material and as the radiation travels through the layers it is focused into a point.[37,45,47–49] Here, in stark contrast, when radiation from a point source is incident on our layered structure a collimated beam can be generated as the output. Thus, this concept is similar to that of a slit, but there are key differences. With a slit, diffraction patterns are generated, and the angle of the output beam is entirely dependent on the location of the source. We will see that with the quartz layers, the existence and angle of the output beam depends on the direction of the anisotropy axis of the quartz films and the frequency of the source. This effect could be used as a demultiplexer where light incident at all angles, such as that from a point source, is collimated in a particular direction which can be controlled with the frequency of the incident waves.

2. Background: Hyperbolic Nature of Bulk Quartz with a Rotated Anisotropy Axis

We start by revisiting the hyperbolic nature of single crystal quartz in order to understand the values of ω and k for which propagation is allowed in the quartz layers. If we take the anisotropy axis to be along z, the uniaxial permittivity tensor can be written as,[45]

$$\overleftrightarrow{\varepsilon}(\omega) = \begin{pmatrix} \varepsilon_{\perp} & 0 & 0 \\ 0 & \varepsilon_{\perp} & 0 \\ 0 & 0 & \varepsilon_{\parallel} \end{pmatrix}. \quad (1)$$

In the frequency range we will explore here, 410 cm^{-1} $< \omega/2\pi c <$ 610 cm^{-1}, there are multiple regions where $\varepsilon_{\perp}$and $\varepsilon_{\parallel}$ have opposite signs, the key feature of a hyperbolic material.[50]

The simple tensor shown above changes quite substantially when we rotate the anisotropy axis in the xz plane by an angle φ. It gains new off-diagonal elements. Using Maxwell's equations[51] we can find a dispersion relation for transverse magnetic (TM) modes where the wavevector perpendicular to the surface of the film, $k_{\perp}$, in crystal quartz is given by

$$k_{\perp} = \frac{-\varepsilon_{xz}k_{\parallel} \pm \sqrt{(\varepsilon_{xz}^2 - \varepsilon_{zz}\varepsilon_{xx})k_{\parallel}^2 + k_0^2(\varepsilon_{xx}\varepsilon_{zz}^2 - \varepsilon_{xz}^2\varepsilon_{zz})}}{\varepsilon_{zz}}. \quad (2)$$

Here, $k_{\parallel}$ is the parallel wavevector and can take any value and $k_0 = \omega/c$ where c is the speed of light. It is important to note that the $k_{\perp}$ value depends on the sign of the wavevector $k_{\parallel}$. This will lead to asymmetric transmission as we will see later on. We proceed by noting that each dielectric constant is a complex number so in general, and when taking damping into account, $k_{\perp}$ will always have real and imaginary components. In the absence of damping, and assuming no rotation of the anisotropy axis, $k_{\perp}$ is either wholly real, allowing for propagation to take place, or wholly imaginary where propagation is not allowed.

When a rotation of the anisotropy axis is introduced however, this condition no longer holds true. For instance, in the absence of damping, the term outside the square root in Eq. (2) always exists and is always wholly real. This means that even if the square root yields a wholly imaginary number, the value of $k_{\perp}$ can still have both real and imaginary parts, meaning waves are still attenuated in this region. In Fig. 1., we create a map of propagation regions (where $k_{\perp}$ is wholly real) and attenuation regions (where $k_{\perp}$ is complex) as a function of $k_{\parallel}$ and ω for

rotation angles of $\varphi = 60°$ and $\varphi = -10°$. This clearly indicates the edges of the bulk bands, i.e. the regions where propagation is allowed.

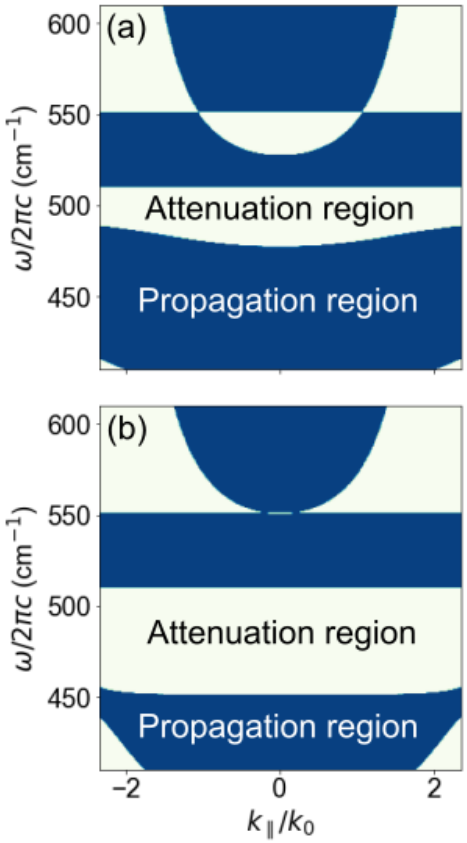

Fig. 1. Bulk band edges for bulk crystal quartz with its anisotropy direction rotated by (a) $\varphi = 60°$ and (b) $\varphi = -10°$. The light regions correspond to the presence of an imaginary part of $k_\perp$ while the darker regions correspond to a $k_\perp$ wholly real.

From Fig. 1., we can identify the regions where transmission is expected to be large, i.e. the propagation regions ($k_\perp$ is wholly real), and where the transmission is expected to be small, i.e. the attenuation regions ($k_\perp$ is complex). In the absence of damping, the bulk bands are symmetric, i.e. the values for $+k_\parallel$ and $-k_\parallel$ are identical. More generally, positive or negative rotations of the anisotropy axis are equivalent, for example, a rotation of $\varphi = -60°$ would have the same bulk band edges as the rotation of $\varphi = +60°$ does.

3. Results

To investigate wave propagation, and as a way to control it, we consider a four-layered structure comprising two layers of crystal quartz sandwiched between air as seen in Fig. 2.

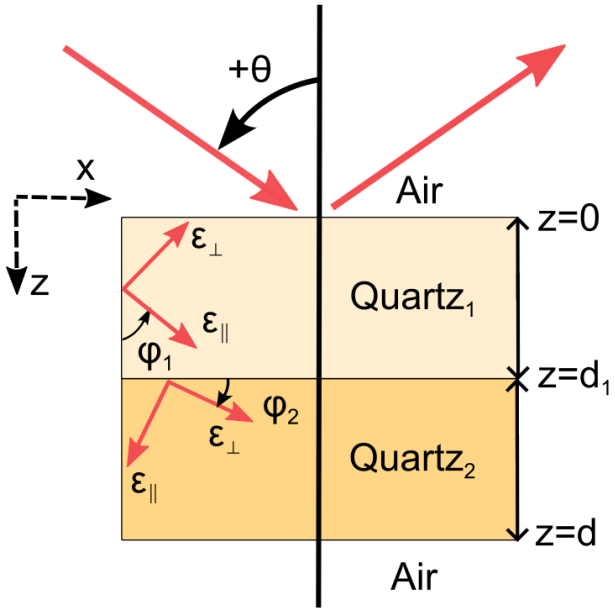

Fig. 2. Geometry for reflection, transmission and absorption calculations. $z = 0$ is chosen to be at the Air/Quartz$_1$ interface, the Quartz$_1$/Quartz$_2$ interface is at $z = d_1$ and the bottom Quartz$_2$/Air interface is at $z = d$. Quartz$_1$ is rotated to $\varphi_1 = 60°$ and is 1.25 microns thick and Quartz$_2$ is rotated to $\varphi_2 = -10°$ and is also 1.25 microns thick.

The z direction is chosen to be perpendicular to the interfaces and the xy plane is the plane of incidence. The first crystal quartz layer, Quartz$_1$, extends from $z = 0$ to $z = d_1$, and the second quartz layer, Quartz$_2$, extends from $z = d_1$ to $z = d$. Through this paper, we will use Quartz$_1$ always to refer to the top quartz layer and assume it to have a rotation of $\varphi_1 = 60°$ and thickness of 1.25 microns. Similarly, Quartz$_2$ always refers to the bottom quartz layer with a rotation of $\varphi_2 = -10°$ and thickness of also 1.25 microns. We consider the electromagnetic waves propagating through this system to be TM so that their behavior can be expressed as a function of the $\boldsymbol{H}$ field, more specifically, as a sum of upward and downward propagating

waves. With this, we can find our electric fields from Maxwell's equations[51] and subsequent transmission, reflection, and even absorption coefficients. Full details are given in Appendices A and B.

3.1 Transmission, Reflection, and Absorption in Quartz Films

We start exploring wave propagation by looking at differences in transmission between single quartz films and the structure with two quartz layers shown in Fig. 3. In Fig. 3(a), we show transmission for a single quartz film of thickness 2.5 μm as a function of incident angle and frequency for the case where the anisotropy axis is rotated by $\varphi_1 = 60°$. Irrespective of the incident angle, there is a large transmission for wavenumbers between 410 cm^{-1} and 460 cm^{-1} or between 550 cm^{-1} and 610 cm^{-1}. This corresponds to the propagation regions in Fig. 1(a). For wavenumbers between 460 cm^{-1} and 500 cm^{-1} we have a band gap and there is no transmittance, this corresponds to an attenuation region in Fig. 1(a). An interesting case occurs for wavenumbers between 500 cm^{-1} and 550 cm^{-1} where there is transmittance for some incident angles and not for others. At the upper limit of this frequency range, there is signficant transmission for negative incident angles, but at the lower bound, the transmission occurs for large positive incident angles, with a smooth transition between the two. This asymmetric transmission is explained in Ref. [45].

Fig. 3(b) plots a transmission map for a thin quartz film, again as a function of frequency and incident angle and of thickness 2.5 μm, but now the anisotropy axis is rotated by $\varphi_2 = -10°$. Similar to Fig. 3(a) there are high transmission frequencies which match with the propagation regions in Fig. 1(b). From 490 cm^{-1} to 550 cm^{-1}, we have high transmission across all incident angles except near 550 cm^{-1}, where there is only a bottleneck region of small positive incident angles with high transmission. This bottleneck has interesting consequences. If we imagine incident light coming in at all possible angles, there will be only transmission at a small set of

output angles, from about 10° to 20°. For wavenumbers between 450 cm^{-1} and 500 cm^{-1} there is a band gap and with no transmittance, which corresponds to an attenuation region in Fig. 1(b).

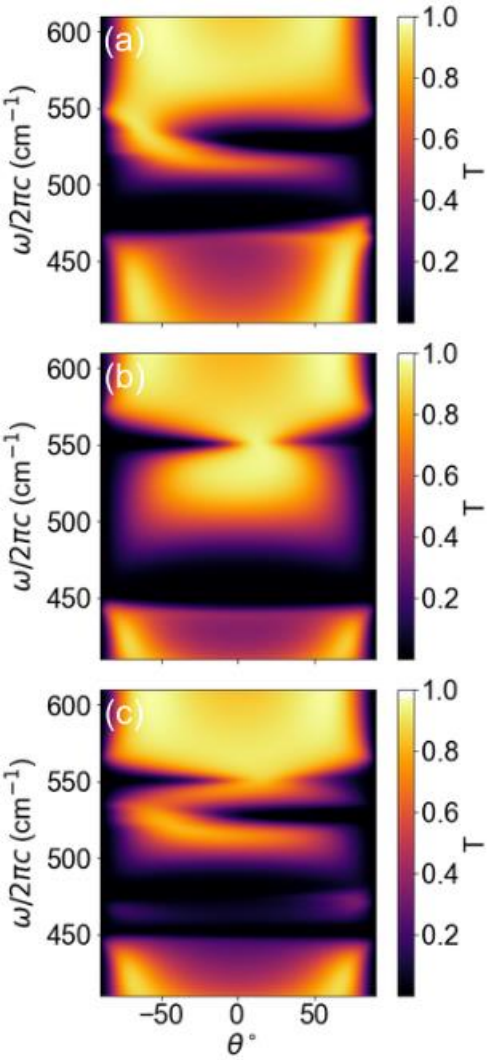

Fig. 3. Energy transmission coefficient as a function of wavenumber and incident angle for various structures. (a) Air/Quartz/Air where the quartz is rotated to $\varphi_1 = 60°$ and is 2.5 microns thick, (b) Air/Quartz/Air where the quartz is rotated to $\varphi_2 = -10°$ and is 2.5 microns thick and (c) Air/$Quartz_1$/$Quartz_2$/Air. Here each of the quartz films is 1.25 microns thick.

In Fig. 3(a), we found that a positive rotation of the anisotropy axis results in transmission for negative incident angles for wavenumbers near 550 cm^{-1}. In general, this is true for any

positive anisotropy axis rotation at wavenumbers near 550 cm^{-1}. In contrast, in Fig. 3(b), where there is a negative rotation of the anisotropy axis, this same frequency region has transmission only for positive incident angles.. Similarly, this occurs, in general, for all negative anisotropy axis rotations. Fig. 3(c) shows the transmittance for a structure of two quartz films, each 1.25 microns thick (for an overal thickness of 2.5 μm), with the upper quartz film having a rotation of the anisotropy axis of $+60°$ and the lower film having a rotation of $-10°$. The results in Fig. 3(c) illustrate that it is possible to use the features of the individual films to engineer a frequency selector where at one frequency ($\omega/2\pi c \approx 550$ cm^{-1}) there is transmission for positive incident angles and the waves at negative incident angles are blocked, while the opposite occurs at a second, nearby, frequency ($\omega/2\pi c \approx 530$ cm^{-1}).

To better understand the transmission results for Fig. 3(c), in Fig. 4., we present the reflection and absorption spectra of the structure with the two quartz layers. In Fig. 4(a), we find that the two quartz film structure gives a symmetric reflection spectrum. The reflection is generally small but can be large in the attenuation region, which is located between 480 cm^{-1} and 500 cm^{-1}. The reflection is also large for very large positive and negative incident angles ($\theta \approx \pm 90°$) where the incident wave is nearly parallel to the surface.

Fig. 4(b), shows the absorption spectrum. The absorption is large for wavenumbers between 450 cm^{-1} and 480 cm^{-1}. Interestingly this is where the transmission map of one quartz film is in an attenuation region and the other is in a propagation region. We point out however that Fig. 1. is for the special case where there is no damping in the material and thus is limited in its applicability. The absorption is also large for positive angles around 530 cm^{-1} and for several spectral regions, but more prominetly also at around 530 cm^{-1}, the absorption is largely asymmetric with respect to the incident angle. This is consistent with the fact that the reflectivity for the system is symmetric. Therefore, indicating that for asymmetric transmission

such as that shown in Fig. 3(d), radiation needs to be absorbed by the material in an asymmetric manner.

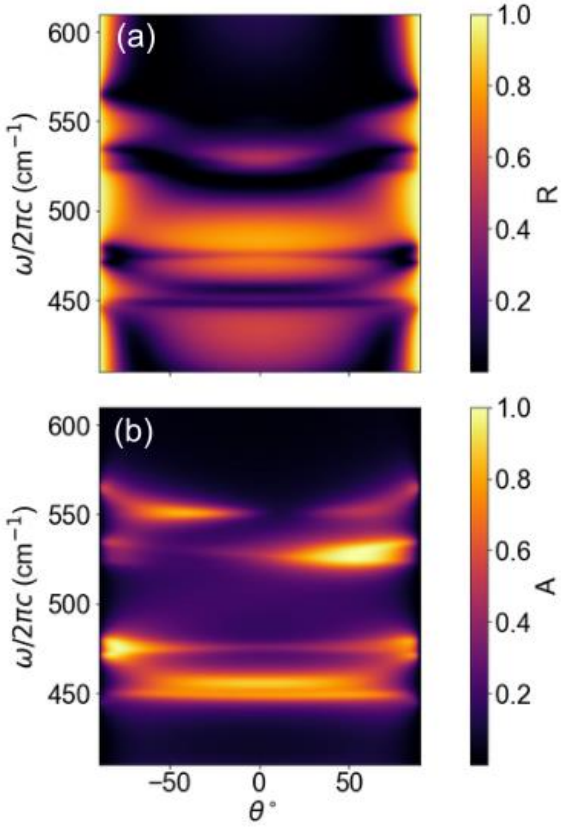

Fig. 4. Reflection and absorption results for the two-quartz structure. (a) Energy reflection coefficient map as a function of incident angle and wavenumber; (b) absorption map as a function of incident angle and wavenumber. The reflection results are independent of the sign of the angle of incidence; however, the absorption is not.

3.2 Propagation of a Beam

To further explore the nature of the asymmetric transmission, we consider the behavior of a Gaussian beam incident on the two-quartz structure. The magnitude of the time-averaged Poynting vector will be used to quantify these effects with further details for the calculation given in Appendix D.

The result of whether a beam is transmitted or absorbed by the two-layered system is already known from the transmission map calculation. The analysis of the Gaussian beam, which is constructed with a plane wave Fourier sum, adds information about what occurs in each quartz film i.e. the location of the absorption, which the transmission map cannot give for the multi-layered quartz structure. We present results of this calculation for four cases (two angles at two frequencies) in Fig. 5.

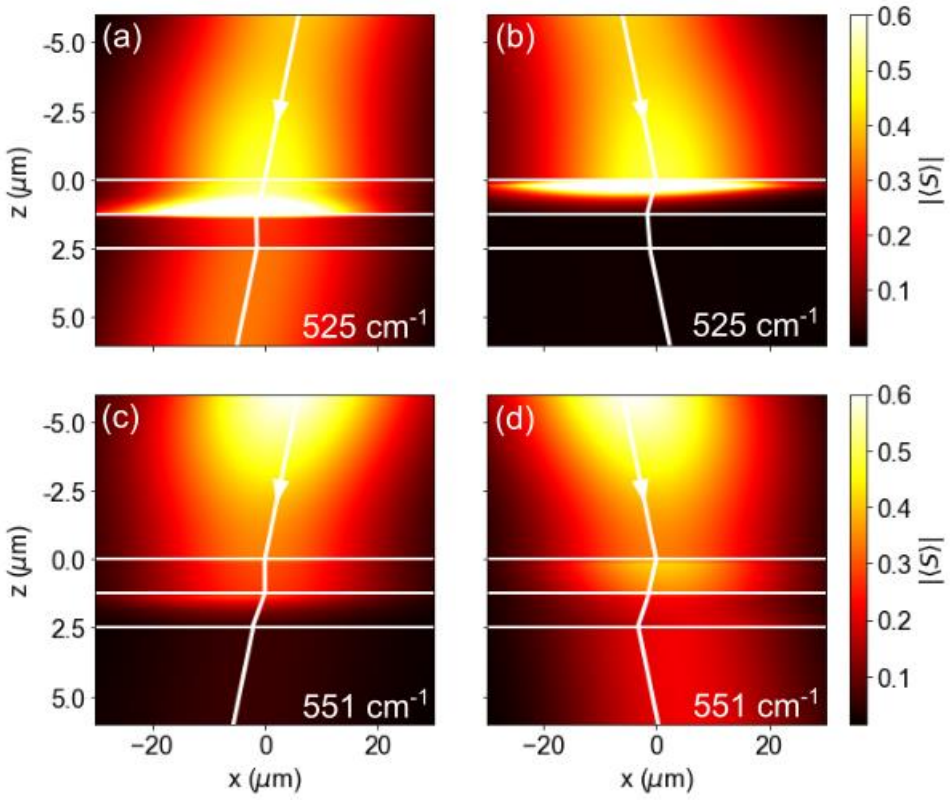

Fig. 5. Intensity profiles in the double quartz structure, with a Gaussian beam of width of $g = 20$ μm at (a) $\theta = -45°$, wavenumber of 525 cm^{-1}, (b) $\theta = 45°$, wavenumber of 525 cm^{-1}, (c) $\theta = -45°$, wavenumber of 551 cm^{-1} and (d) $\theta = 45°$, wavenumber of 551 cm^{-1}. The thicker white lines are the path of the beam obtained from geometry and the incident and refracted angles, given in Eq. (D.7). The horizontal white lines are the Quartz layers. The top line is at $z = 0$ μm, the middle line is at $z = 1.25$ μm and the bottom line is at $z = 2.5$ μm. Quartz$_1$ is between the top two lines and Quartz$_2$ is between the bottom two lines.

Fig. 5(a) shows the behavior of a Gaussian beam at 525 cm^{-1} and an incident angle of $\theta = -45°$. Interestingly, the magnitude of the time-averaged Poynting vector is largest in the top quartz film, $Quartz_1$, instead of the incident air. To explain this, consider the components: H_y, E_x and E_z, which are used to calculate $|\langle \boldsymbol{S} \rangle|$ (see Eq. (D.6) in Appendix D). Here, the z component of the electric field drives the large power flow, and it corresponds to the x component of the power flow, as the magnetic field is only in the y direction. Thus, in addition to transmission of the beam through the structure, there is a lot of power traveling parallel to the surface at the Air/$Quartz_1$ interface and throughout $Quartz_1$. Another feature of note is that the beam undergoes negative refraction as it passes between the quartz layers. We note that negative refraction is key to planar slab lens structures.[52,53]

In contrast, in Fig. 5(b), a beam also at 525 cm^{-1}, is shown to be absorbed when incident at the opposite angle of $\theta = +45°$. The absorption occurs in $Quartz_1$ and the beam is negatively refracted into this medium. Similarly, to Fig. 5(a), there is a lot of power traveling parallel to the surface of the Air/$Quartz_1$ interface. Interestingly, this behavior can be readily reversed when the wavenumber is changed to 551 cm^{-1}, as in Fig. 5(c), where the beam incident at $\theta = -45°$ is negatively refracted into $Quartz_2$ and absorbed. On the other hand, the beam is transmitted when incident at $\theta = +45°$. These two frequencies where transmission is not only strongly asymmetric and direction-dependent but also reversible, enable our two-layered quartz structure to function as a frequency selector.

The lack of transmission in Figs. 5(b) and 5(c) is remarkable. To understand this, it is helpful to look at the wavelengths and penetration depths in the films for the different cases. The effective wavelength normal to the films is calculated by $\lambda = 2\pi/\mathrm{Re}|k_\perp|$. We find for all the various cases that these wavelengths range from 3 microns to over 100 microns. Since these values are larger than the film thicknesses, we do not expect that the lack of transmission is

due to destructive interference. In contrast, the penetration depth, given by $\delta = 1/\mathrm{Im}|k_{b\perp}|$, for the top quartz film in Fig. 5(b) is 0.6 microns and is 24.3 microns for the bottom quartz film. These values are consistent with the lack of transmission for that case. In Fig. 5(a) the penetration depth for the top quartz film is 32.4 microns and for the bottom quartz film it is 41.1 microns; these large penetration depths indicate why transmission occurs in this case. Similar behaviors occur for the cases shown in Figs. 5(c) and 5(d).

3.3 All-Angle Propagation

Now that we have examined how a beam travels through our structure, we turn to the behavior of a radiating line current source[47], which accounts for beams travelling at every incident angle. While this is typically used to explore radiation focusing and image formation due to all-angle negative refraction,[37] here the outcome is not so obvious due to the asymmetric nature of the propagation with respect to the travelling direction. To investigate this, we model an oscillating source centered at $x = 0, z = -20\ \mu$m, so that it is placed 20 microns above the two-quartz structure with details of the calculation provided in Appendix D. We use this approach to probe behavior at the two wavenumbers considered in Fig. 5., which are the wavenumbers at which there are narrow regions of transmission angles [see Fig. 3(c)].

In Fig. 6(a), incident light at 525 cm^{-1} is transmitted only at negative angles and collimated into a beam of light. We note that due to the different length scales for the vertical and horizontal axes, the transmitted beam looks nearly normal to the interface; the actual angle is centered around $-60°$. In contrast, at 551 cm^{-1}, transmission only occurs at positive angles as seen in Fig. 6(b). Here, the output collimated beam is centered around $+20°$. Hence, the angle of the output collimated beams depends on the frequency of the source and anisotropy axis angles of the layered quartz structure. This is remarkable because the incident source is composed of light with every incident angle, and it uniformly illuminates the quartz structure. The result is

a collimated, transmitted beam that flows with a distinct angle. It is interesting to note that the collimated beam is actually slightly narrower than the uniformly illuminated surface region. Again, the structure with two quartz films allows this to be used as a frequency selector.

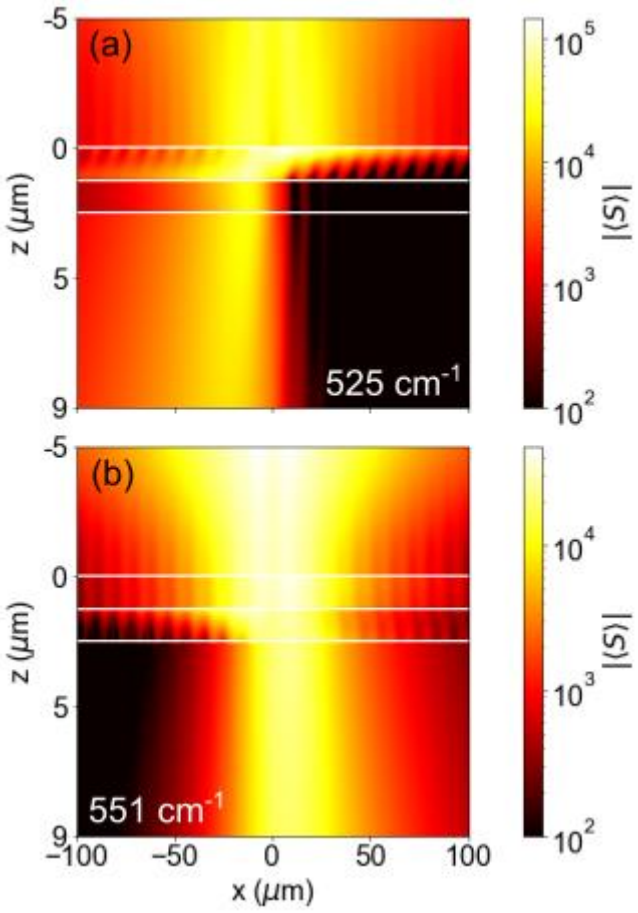

Fig. 6. Power flow through the double quartz structure from a radiating line current source centered at $x = 0, z = -20\ \mu$m for the wavenumbers (a) 525 cm^{-1} and (b) 551 cm^{-1}. The magnitude of the time-averaged Poynting vector is in arbitrary units. As with the geometry in Fig. 2., Quartz$_1$ is between the white lines at $z = 0$ and $z = 1.25\ \mu$m and Quartz$_2$ is between the white lines at $z = 1.25$ and $z = 2.5\ \mu$m. Note the transmission directions in the figure are somewhat misleading because of the different scales for the horizontal and vertical axes.

3.4 Other Geometries

The two-quartz structure sandwiched between air layers is an ideal configuration to explore effects that are related to high transmission. If effects related to high reflection instead of transmission are of interest, other geometries are better suited for this investigation. For instance, a geometry that allows wavevectors to be greater than the light line will maximize these effects. The attenuated total reflection (ATR) experiment[54] in an Otto-like configuration[55] is one such geometry.

The ATR experiment emphasizes surface polaritons, which occur outside of the light line. To calculate propagation in an ATR geometry, a dielectric prism is placed above the $Quartz_1$/$Quartz_2$ structure with the thicknesses considered earlier. The prism is chosen to have a dielectric constant of 5.5 and is placed 2.5 microns above $Quartz_1$. Since the dielectric prism has a permittivity much greater than that of air, this yields total internal reflection for angles larger than the critical angle of $\theta = \arcsin\left(1/\sqrt{5.5}\right) = \pm 25.24°$. For these larger angles, any dips in the reflectivity spectra can have two origins. They can be caused by an evanescent wave in the gap region below the prism coupling to a surface polariton of the quartz structure or when the thin quartz films act as a waveguide and the evanescent wave couples to bound polariton states inside the thin films. The reduction from the usual total internal reflection arises because these waves carry energy away from the incident beam. Here, the energy transmission coefficient cannot be calculated by simply using $T = tt^{\star}$ because the incident (prism) and transmitted (air) media are different. The details of the calculation are outlined in Appendix C.

In Fig. 7(a), the ATR reflection map as a function of incident angle and wavenumber is plotted for the geometry indicated in the paragraph above. One sees both surface and guided wave modes indicated by dips in the reflectivity outside the critical angle. These modes, with wavenumbers between 450 cm^{-1} and 550 cm^{-1}, are important for signal processing applications and biological sensing applications[56,57] and correspond to band gaps in the transmission spectra.[58] As seen in Fig. B.1. in Appendix B, this reflection map is a combination of the two single quartz ATR maps. Thus, it is easy to engineer a structure to have modes at any desired frequency by using quartz films with different rotation angles.

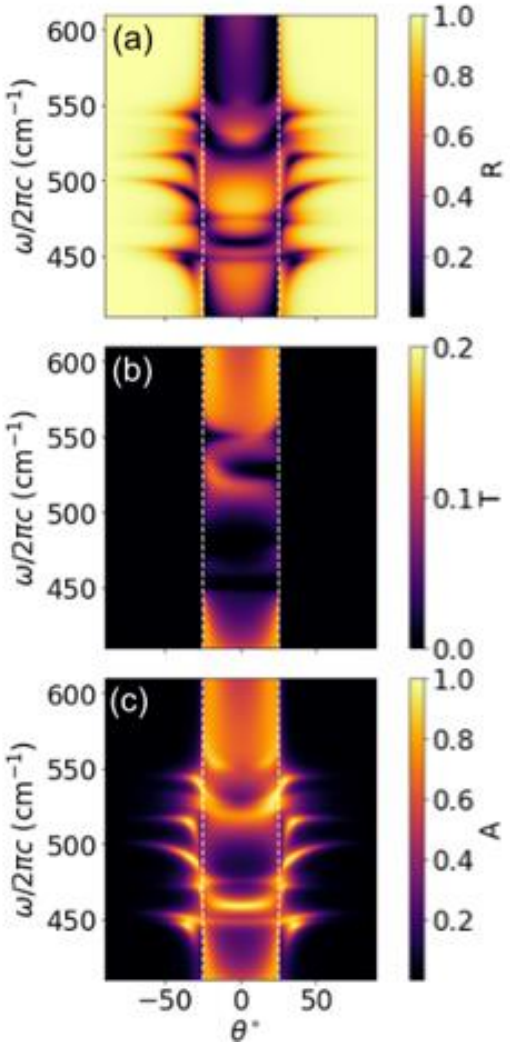

Fig. 7. Reflection, transmission and absorption results for the two-quartz structure in the ATR geometry. (a) Energy reflection coefficient map (b) energy transmission coefficient map (plotted with a different color bar scale); and (c) absorption map, each as a function of incident

angle and wavenumber. The reflection results are independent of the sign of the angle of incidence; however, the transmission and absorption are not. The dashed, white vertical lines represent the critical angle.

The energy transmission coefficient is considered in Fig. 7(b) for the ATR configuration. The coefficient is small everywhere and only nonzero for light incident at an angle smaller than the critical angle. In this restricted region, the asymmetric transmission pattern is found to be similar to what was found previously in Fig. 3(c), however the intensity is much weaker (note that the scale here is much smaller than the other panels).

The absorption in the ATR geometry is depicted in Fig. 7(c). It is large for all bulk, surface and guided modes present in the reflection spectrum of Fig. 7(a). We also notice that it is asymmetric for angles between $\pm\theta$, consistent with the asymmetric transmission spectra.

4. Conclusion and Discussion

Greater control over the asymmetric transmission in crystal quartz structures was found by using a double quartz film system. This is possible by combining positive and negative rotations of the anisotropy axis within two thin quartz films. The thicknesses are chosen so that the structure is not too thick as to block transmission and not too small as to transmit everything. This led to new transmission patterns where multiple frequencies were found to have bottleneck regions i.e. only allowing propagation of a small section of incident angles. The asymmetry in the propagation direction of the transmitted light can be used to separate the frequencies and create a demultiplexer.

Because the asymmetry observed seems to stem from highly asymmetric absorbing regions, we expect that this can lead to asymmetric heating as energy is stored inside the material. As such, it would be worthwhile to consider temperature effects and the subsequent ramifications on the properties of the thin quartz layers in a future study. For instance, this could be an avenue

for investigations of angle-controlled, near field radiative heat transfer.[59,60] Even more fruitful would be to consider magneto-optical materials such as indium antimonide (InSb), a magnetised plasma that has temperature dependent dielectric constants.[61] For example, an incident laser light might initially be absorbed by an InSb film, which in turn would cause the film to heat up and its permittivity to change. At a later time, the new permittivity could permit transmission of the light. There are many other intriguing possibilities such as stacking InSb and quartz films. These possiblities may lead to self-induced transparency where the incident pulse propagates through the material without disperision or decay.[62] These photothermal effects have been demostrated in microscopes[63] and a dielectric microcavity.[64]

In the current study, the selected output angle is controlled by the frequency of the incident light and the rotation of the anisotropy axis. However, once the structure is created, there is no more tunability due to the rotation of the anisotropy axis rotation. More tunability can be achieved in other hyperbolic materials like liquid crystals with applied fields.[65] This would be a worthwhile endeavor as liquid crystals have already been proven to create fast, tunable filters.[66]

Lastly, in the Otto-like ATR configuration, control over the location and quantity of surface and guided modes was observed. While, this system also displayed a faint asymmetric transmission pattern, all reflection spectra were symmetric. An asymmetric, angle controllable reflection spectra, can be introduced by considering reflections where the plane of incidence is not simply the xz plane. In this case, the reflection asymmetry comes from a cross-polarization conversion between TM and transverse electric (TE) waves.[67] It would be noteworthy to discover the kinds of asymmetric transmission and absorption possible with an asymmetric reflection spectrum.

Appendices

SI units are used throughout this paper and temperature effects are neglected.

Appendix A. Determining the Relative Permittivity

The components of the permittivity tensor can be found using

$$\varepsilon_u = \varepsilon_{\infty,u} \prod_m \left(\frac{\omega_{Lm,u}^2 - \omega^2 - i\omega\gamma_{Lm,u}}{\omega_{Tm,u}^2 - \omega^2 - i\omega\gamma_{Lm,u}} \right), \qquad (A.1)$$

where u represents either the ∥ (extraordinary) or ⊥ (ordinary) axis, ω is the frequency, $\varepsilon_{\infty,u}$ is the dielectric constant at infinity, $\omega_{Tm,u}$ is the frequency of the transverse optical phonons, $\omega_{Lm,u}$ is the frequency of the longitudinal optical phonons and $\gamma_{Tm,u}$ and $\gamma_{Lm,u}$ are the damping parameters of the m^{th} transverse or longitudinal optical phonon mode, respectively [48]. In this work we have used the parameters found by Gervais and Piriou,[68] neglecting their experimental artefact,[48,68,69] to evaluate the dielectric constants in Eq. (A.1).

To take into account the rotation of the crystal axes with respect to the surface, the relative permittivity tensor given in Eq. (1) is rotated in the xz plane by an angle φ. This transformation is done by: $\overleftrightarrow{\varepsilon'}(\omega) = R(\varphi)\overleftrightarrow{\varepsilon}(\omega)R^{-1}(\varphi)$ where $R(\varphi)$ is the rotation matrix and $R^{-1}(\varphi)$ is its transpose. The result is[45,70]

$$\overleftrightarrow{\varepsilon'}(\omega) = \begin{pmatrix} \varepsilon_{xx} & 0 & \varepsilon_{xz} \\ 0 & \varepsilon_{yy} & 0 \\ \varepsilon_{zx} & 0 & \varepsilon_{zz} \end{pmatrix}, \qquad (A.2)$$

where the rotated dielectric tensor components are:

$$\varepsilon_{\mathrm{xx}} = \varepsilon_{\perp} \cos^2 \varphi + \varepsilon_{\parallel} \sin^2 \varphi \qquad (A.3a)$$

$$\varepsilon_{\mathrm{zz}} = \varepsilon_{\perp} \sin^2 \varphi + \varepsilon_{\parallel} \cos^2 \varphi \qquad (A.3b)$$

$$\varepsilon_{\mathrm{xz}} = \varepsilon_{\mathrm{zx}} = (\varepsilon_{\perp} - \varepsilon_{\parallel}) \cos \varphi \sin \varphi \qquad (A.3c)$$

$$\varepsilon_{yy} = \varepsilon_{\perp} \qquad (A.3d)$$

Appendix B. Fresnel Reflection and Transmission Coefficient Determination

To find the reflection and transmission coefficients using the geometry of Air/Quartz$_1$/Quartz$_2$/Air from Fig. 2., and assuming a TM mode, the $\boldsymbol{H}$-field above and below the sample can be written as

$$\boldsymbol{H} = \hat{y}e^{i(k_{\parallel}x-\omega t)}\left(a_n e^{ik_{n\perp}z} + b_n e^{-ik_{n\perp}z}\right) \qquad (B.1)$$

where a_n and b_n are the amplitudes for the waves in layer n (for the air this $n = 1$ and $n = 4$) propagating along the $+z$ and $-z$ directions, respectively. The amplitude of the incident wave is set as $a_1 = 1$. As the lower air layer is semi-infinite, there is there is only a transmitted wave, which means that $b_4 = 0$. Additionally, $k_{\parallel} = k_0\sqrt{\varepsilon}\sin\theta$, where θ is the incident angle and ε is the dielectric constant of the incident medium.

The perpendicular wavevectors can be derived from the dispersion relation and, in the air are given by

$$k_{\perp}^2 = k_0^2 - k_{\parallel}^2. \qquad (B.2)$$

The situation is different inside the quartz layers because, as can be seen from Eq. (2), there are <u>two</u> different values for the perpendicular wavevector in each film. Thus for $n = 2$ and $n = 3$

$$\boldsymbol{H} = \hat{y}e^{i(k_{\parallel}x-\omega t)}\left(a_n e^{ik_{n_a\perp}z} + b_n e^{ik_{n_b\perp}z}\right) \qquad (B.3)$$

where $k_{n_a\perp}$ and $k_{n_b\perp}$ indicate the two values generated by Eq. (2).

The electric field in each film can be uniquely derived from Maxwell's Equations $\nabla \times \boldsymbol{H} = \partial\boldsymbol{D}/\partial t$ and the constitutive relation $\boldsymbol{D} = \varepsilon_0\overleftrightarrow{\varepsilon}(\omega)\boldsymbol{E}$, where ε_0 is the vacuum permittivity.[71] Doing so, the component of $\boldsymbol{E}$ tangential to the surface and interface layers is found to be

$$E_x = \frac{-1}{\omega\varepsilon_0} e^{i(k_\parallel x - \omega t)} \left(a_n k_{n\perp} e^{ik_{n\perp} z} + b_n k_{n\perp} e^{-ik_{n\perp} z} \right) \qquad (B.4)$$

in the air layers. Similarly, the tangential components in the quartz layers are given by

$$E_x = \frac{-1}{\omega\varepsilon_0} e^{i(k_\parallel x - \omega t)} \left(a_n \alpha_n e^{ik_{n_a\perp} z} + b_n \beta_n e^{ik_{n_b\perp} z} \right) \qquad (B.5)$$

where

$$\alpha_n = \frac{k_\parallel \varepsilon_{xz} + k_{n_a\perp} \varepsilon_{zz}}{\varepsilon_{xz}^2 - \varepsilon_{xx}\varepsilon_{zz}} \qquad (B.6a)$$

$$\beta_n = \frac{k_\parallel \varepsilon_{xz} + k_{n_b\perp} \varepsilon_{zz}}{\varepsilon_{xz}^2 - \varepsilon_{xx}\varepsilon_{zz}} \qquad (B.6b)$$

While the permittivities are not explicitly subscripted, they are, in general, different because the quartz layers have different directions for the anisotropy axes.

The reflection and transmission coefficients are found by equating the tangential components of the electric and magnetic fields at each layer boundary. Doing so the following matrix (for the geometry in Fig. 2.) of the form $Fx = G$ is obtained,

$$\begin{pmatrix} -1 & 1 & 1 & 0 & 0 & 0 \\ k_{1\perp} & -\alpha_2 & -\beta_2 & 0 & 0 & 0 \\ 0 & e^{ik_{2a\perp}d_1} & e^{ik_{2a\perp}d_1} & -e^{ik_{3a\perp}d_1} & -e^{ik_{3_b\perp}d_1} & 0 \\ 0 & \alpha_2 e^{ik_{2a\perp}d_1} & \beta_2 e^{ik_{2a\perp}d_1} & -\alpha_3 e^{ik_{3a\perp}d_1} & -\beta_3 e^{ik_{3a\perp}d_1} & 0 \\ 0 & 0 & 0 & e^{ik_{3a\perp}d} & e^{ik_{3_b\perp}d} & -e^{ik_{1\perp}d} \\ 0 & 0 & 0 & \alpha_3 e^{ik_{3a\perp}d} & \beta_3 e^{ik_{3_b\perp}d} & k_{1\perp} e^{ik_{1\perp}d} \end{pmatrix} \begin{pmatrix} b_1 \\ a_2 \\ b_2 \\ a_3 \\ b_3 \\ a_4 \end{pmatrix} = \begin{pmatrix} 1 \\ k_{1\perp} \\ 0 \\ 0 \\ 0 \\ 0 \end{pmatrix}. \qquad (B.7)$$

Solving Eq. (B.7) for b_1 gives the reflection coefficient r. The reflectance R is found by $R = |r|^2 = rr^\star$. Similarly, Eq. (B.7) is used to solve for a_4 which is the transmission coefficient t. The transmittance T is found by $T = |t|^2 = tt^\star$. The solution to Eq. (B.7) is used to create the transmission and reflection maps in Fig.s 3 and 4.

It is straightforward to extend the above discussion for the ATR geometry discussed in Fig.s 7 and 8. Here, for the dielectric prism, Eq. (B.2) becomes

$$k_{\perp}^2 = \varepsilon_p k_0^2 - k_{\parallel}^2. \qquad (B.8)$$

The ATR results in Fig. 7. are complicated. Many surface and guided modes were found in a 100 cm^{-1} interval of wavenumbers. To help explain where these modes originate, the ATR results for single quartz films is now presented in Fig. B.1.

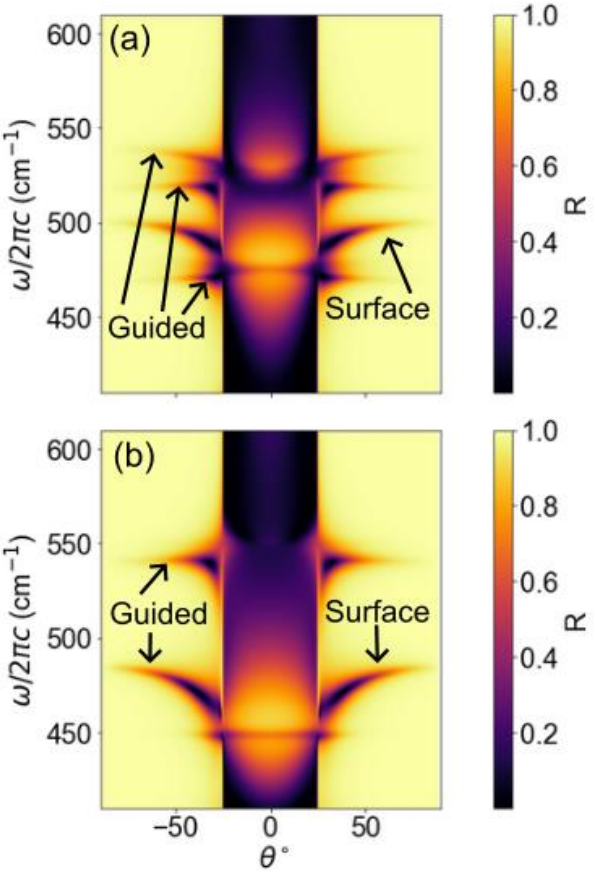

Fig. B.1. Energy reflection coefficient for reflection spectra where the air gap is 2.5 microns thick in the geometries (a) Prism/Air/$Quartz_1$/Air and (b) Prism/Air/$Quartz_2$/Air. The text and arrows identify the modes as surface or guided waves.

These thin films are combined to create the geometry illustrated in Fig. 2. Fig. B.1(a) plots the reflection spectrum for a single 1.25 micron quartz film with an anisotropy axis rotated to 60°.

There are surface and guided modes in the range of wavenumbers between 475 and 540 cm^{-1}. We know that the surface modes occur in the attenuation regions and guided modes occur in the propagating regions, where the bulk polaritons were [72]. A comparison with Fig. 1., easily identifies the modes as such. An anisotropy axis rotation of $-10°$ for a single 1.25 micron quartz film is considered in Fig. B.1(b). Again, a comparison with Fig. 1. shows that there are surface modes in the attenuation regions and guided modes in the propagation regions. There are fewer modes than in Fig. B.1(a). This is because there are more regions in $Quartz_1$ where only one of the components of the dielectric tensor are negative.[73] It is easy to see that these reflection spectrum combine to the spectrum in Fig. 7(a).

Appendix C. Transmission in the ATR Geometry

In the ATR geometry, the incident and transmitted media are different. Consequently, the energy transmission coefficient must be calculated by

$$T = \frac{Z_i \cos\theta_t}{Z_t \cos\theta_i} |t|^2, \qquad (C.1)$$

where θ is the angle of the light with respect to the surface normal and the impedance is $Z = \sqrt{\mu/\varepsilon}$ where the subscripts i and t denote incident and transmitted, respectively.[74] All materials considered in this paper are nonmagnetic, so the impedance reduces to $Z = 1/\sqrt{\varepsilon}$.

The correction to $|t|^2$ is necessary to ensure that energy is conserved. Therefore, any media sandwiched between the incident and transmitted layers are irrelevant for this calculation. Energy conservation requires that the frequency ω and parallel momentum $k_\parallel$ are also conserved. The only unknown in Eq. (C.1) is the transmitted angle, which is determined below.

In the ATR geometry, the dispersion relations are $\omega = ck/\sqrt{\varepsilon_p}$ in the incident prism and $\omega = ck$ in the transmitted air. This gives parallel momenta of: $k_\parallel = \frac{\omega}{c}\sqrt{\varepsilon_p}\sin\theta_i$ in the prism and

$k_{\parallel} = \frac{\omega}{c} \sin\theta_t$ in the air. From conservation of parallel momenta, the incident and transmitted momenta are equated to find a transmitted angle of $\theta_t = \arcsin\left(\sqrt{\varepsilon_p} \sin\theta_i\right)$.

It is obvious that there is a critical angle for any media whose dielectric constant is greater than unity as arcsin is only defined from -1 to $+1$, which is the range of $\sin\theta$. Physically, this is the case of total internal reflection where there is no transmission (aside from an evanescent wave) and corresponds to a transmitted angle of 90°. In the ATR geometry, it is apparent that the quantity $|t|^2$, in Eq. (C.1), can be larger than unity, as the pre-factor is proportional to $\varepsilon_p^{-1/2}$ and is smaller than unity.

When the incident and transmitted media are the same, the incident and transmitted angles are the same. This condition reduces Eq. (C.1) to $T = |t|^2$, as given in the main text. A correction is never necessary to the energy reflection coefficient R because the incident and reflected light propagate in the same medium and the angles are equal in magnitude due to the law of reflection.

Appendix D. Power Flow

Appendix D.1. Gaussian Beams

The Gaussian beam calculation uses the magnitude of the time-averaged Poynting vector. The electric and magnetic fields of the finite beam are similar to what was previously used to calculate the reflection and transmission coefficients, but there are two key differences. Here, the fields are Fourier sums of plane waves. This leads to an integration over all parallel wavevectors. The second difference is that the wave shape must be accounted for.

For a TM mode, in the geometry of Air/Quartz$_1$/Quartz$_2$/Air from Fig. 2., the $\boldsymbol{H}$-field above and below the sample is

$$H_y = \int_{-k_0}^{k_0} \psi(k_\parallel)\left(a_n e^{ik_{n\perp}z} + b_n e^{-ik_{n\perp}z}\right)e^{i(k_\parallel x - \omega t)}dk_\parallel \qquad (D.1)$$

where the wave shape $\psi(k_\parallel)$ for a Gaussian beam is given by

$$\psi(k_\parallel) = \frac{-g}{2\cos\theta\sqrt{\pi}}\exp\left[\frac{-g^2(k_\parallel - k_0\sin\theta)^2}{4\cos^2\theta}\right] \qquad (D.2)$$

where g is the beam width, θ is the beam's incident angle and the beam is centered at $x = 0, z = 0$. Note that $\psi(k_\parallel)$ is the same in each layer.[47,48,75]

The corresponding $\boldsymbol{E}$-fields above and below the sample are uniquely determined from Maxwell's equations[51] to be

$$E_x = \int_{-k_0}^{k_0} \frac{k_{n\perp}}{\omega\varepsilon_0}\psi(k_\parallel)\left(a_n e^{ik_{n\perp}z} - b_n e^{-ik_{n\perp}z}\right)e^{i(k_\parallel x - \omega t)}dk_\parallel \qquad (D.3a)$$

$$E_z = \int_{-k_0}^{k_0} -\frac{k_\parallel}{\omega\varepsilon_0}\psi(k_\parallel)\left(a_n e^{ik_{n\perp}z} + b_n e^{-ik_{n\perp}z}\right)e^{i(k_\parallel x - \omega t)}dk_\parallel\,, \qquad (D.3b)$$

and for the same reasons presented in the Fresnel coefficient calculations section, it is assumed that $a_1 = 1$ and $b_4 = 0$.

In the quartz films, the fields are given by

$$H_y = \int_{-k_0}^{k_0} \psi(k_\parallel)\left(a_n e^{ik_{n_a\perp}z} + b_n e^{ik_{n_b\perp}z}\right)e^{i(k_\parallel x - \omega t)}dk_\parallel \qquad (D.4a)$$

$$E_x = \int_{-k_0}^{k_0} \frac{-1}{\omega\varepsilon_0}\psi(k_\parallel)\left(\alpha_n a_n e^{ik_{n_a\perp}z} + \beta_n b_n e^{ik_{n_b\perp}z}\right)e^{i(k_\parallel x - \omega t)}dk_\parallel \qquad (D.4b)$$

$$E_z = \int_{-k_0}^{k_0} \frac{1}{\omega\varepsilon_0}\psi(k_\parallel)\left(\alpha_{nz} a_n e^{ik_{n_a\perp}z} + \beta_{nz} b_n e^{ik_{n_b\perp}z}\right)e^{i(k_\parallel x - \omega t)}dk_\parallel \qquad (D.4c)$$

where α_n and β_n are still defined by Eqs. (B.6a) and (B.6b), respectively, and

$$\alpha_{nz} = \frac{k_{\parallel}\varepsilon_{xx} + k_{n_a\perp}\varepsilon_{xz}}{\varepsilon_{xz}^2 - \varepsilon_{xx}\varepsilon_{zz}} \qquad (D.5a)$$

$$\beta_{nz} = \frac{k_{\parallel}\varepsilon_{xx} + k_{n_b\perp}\varepsilon_{xz}}{\varepsilon_{xz}^2 - \varepsilon_{xx}\varepsilon_{zz}}. \qquad (D.5b)$$

where $k_{n_a\perp}$ and $k_{n_b\perp}$ are again obtained from Eq. (2) and $k_{\perp}$ is given by Eq. (B.2). Again, as in Eqs. (B.6a) and (B.6b), while the permittivities are not subscripted, they are, in general, different because the quartz layers have different anisotropy axes.

As was done previously, the coefficients in Eqs. (D.1), (D.3) and (D.4) are determined by solving the set of linear equations obtained by equating the tangential $\boldsymbol{E}$ and $\boldsymbol{H}$ fields at each boundary.

In principle, the integrals in Eqs. (D.1), (D.3) and (D.4) are over all wavevectors, but practically, the integral can be restricted to $-k_0 \leq k_{\parallel} \leq k_0$. The restriction excludes the evanescent $k_{\parallel}$ values because the incident Gaussian beam propagates in air.[53,76] However, this restriction will not always give a symmetric Gaussian for $\psi(k_{\parallel})$. That is not problematic because a shifted Gaussian would include evanescent $k_{\parallel}$ values and miss important $k_{\parallel}$ values. The inclusion of evanescent parallel wavevectors would yield unphysical solutions.

To evaluate the integrals numerically, the interval is split into an odd number of equally spaced sites, which gives an even number of divisions. This allows their computation by Simpson's 1/3 Rule.[77] Additionally, it is done for a time $t = 0$ and time evolution is neglected. The Gaussian beam result is quantified with the magnitude of the time-averaged Poynting vector given by:[75]

$$|\langle S \rangle| = \frac{1}{2}\sqrt{\mathrm{Re}\left(E_z H_y^{\star}\right)^2 + \mathrm{Re}\left(E_x H_y^{\star}\right)^2}. \qquad (D.6)$$

The direction of the power flow is determined by considering the angle of refraction between each media. This must be done with the Poynting vector[78] and not from the angle between $k_\perp$ and $k_\parallel$, as $\boldsymbol{k}$ and $\boldsymbol{S}$ are not generally in the same direction.[48,76] From the time-averaged Poynting vector, $\langle \boldsymbol{S} \rangle = 1/2\ \mathrm{Re}(\boldsymbol{E} \times \boldsymbol{H}^\star)$, the angle of refraction is

$$\tan\theta = \frac{\langle S_x \rangle}{\langle S_z \rangle} = \frac{\mathrm{Re}(k_\parallel \varepsilon_{xz} + k_\perp \varepsilon_{zz})}{\mathrm{Re}\left(k_\parallel \varepsilon_{xx} + k_{n_b \perp} \varepsilon_{xz}\right)}, \tag{D.7}$$

where $k_\perp$ is given in Eq. (B.2).

Appendix D.2. Radiating Line Current Source

Our oscillating line current source is an infinite source in the y direction that radiates in every direction of the xz plane. This source is composed of an oscillating line of magnetic current K directed along the y axis at $x = 0, z = -20\ \mu\mathrm{m}$. The implementation is the same as with the Gaussian beam, but with a wave shape of [47,79]

$$\psi(k_\parallel) = -\frac{\omega \varepsilon_0 K}{4\pi k_\perp}, \tag{D.8}$$

where $k_\perp$ is given by Eq. (B.2). Note that Eq. (D.8) goes to infinity at the source's center. Additionally, the $e^{ik_\perp z}$ terms in Eqs. (D.1), (D.3) and (D.4) are shifted to account for the initial height of the source.

References

1. Wood, R. W. On a remarkable case of uneven distribution of light in a diffraction grating spectrum. *Proc. Phys. Soc. London* **18**, 269 (1902).

2. Mills, D. L. & Burstein, E. Polaritons: the electromagnetic modes of media. *Reports Prog. Phys.* **37**, 817 (1974).

3. Tolpygo, K. B. Physical Properties of a Rock Salt Lattice Made Up of Deformable Ions. *Zh. Eksp. Teor. Fiz.* **20**, 497–509 (1950).

4. Huang, K. Lattice Vibrations and Optical Waves in Ionic Crystals. *Nature* **167**, 779–780 (1951).

5. Born, M. & Huang, K. *Dynamical theory of crystal lattices*. *Dynamical Theory of Crystal Lattices* (Clarendon Press, 1954).

6. Hopfield, J. J. Theory of the contribution of excitons to the complex dielectric constant of crystals. *Phys. Rev.* **112**, 1555–1567 (1958).

7. Huang, K. On the interaction between the radiation field and ionic crystals. *Proc. R. Soc. London. Ser. A. Math. Phys. Sci.* **208**, 352–365 (1951).

8. Camley, R. E. & Mills, D. L. Surface polaritons on uniaxial antiferromagnets. *Phys. Rev. B* **26**, 1280 (1982).

9. Jensen, M. R. F., Feiven, S. A., Parker, T. J. & Camley, R. E. Experimental determination of magnetic polariton dispersion curves in FeF2. *Phys. Rev. B* **55**, 2745 (1997).

10. Abraha, K., Smith, S. R. P. & Tilley, D. R. Surface polaritons and attenuated total reflection spectra of layered antiferromagnets in the Faraday configuration. *J. Phys.*

Condens. Matter **7**, 6423 (1995).

11. Burke, J. J., Stegeman, G. I. & Tamir, T. Surface-polariton-like waves guided by thin, lossy metal films. *Phys. Rev. B* **33**, 5186–5201 (1986).

12. Berini, P. Plasmon-polariton waves guided by thin lossy metal films of finite width: Bound modes of asymmetric structures. *Phys. Rev. B* **63**, 125417 (2001).

13. Andrew, P. & Barnes, W. L. Energy Transfer Across a Metal Film Mediated by Surface Plasmon Polaritons. *Science (80-.).* **306**, 1002–1005 (2004).

14. Le Gall, J., Olivier, M. & Greffet, J.-J. Experimental and theoretical study of reflection and coherent thermal emissionby a SiC grating supporting a surface-phonon polariton. *Phys. Rev. B* **55**, 10105 (1997).

15. Tyboroski, M. H., Anderson, N. R. & Camley, R. E. An effective medium study of surface plasmon polaritons in nanostructured gratings using attenuated total reflection. in *Journal of Applied Physics* vol. 115 013104 (2014).

16. Tyboroski, M., Macêdo, R. & Camley, R. E. Nonreciprocity in millimeter wave devices using a magnetic grating metamaterial. *Phys. Rev. Mater.* **5**, 115201 (2021).

17. Camley, R. E. & Mills, D. L. Collective excitations of semi-infinite superlattice structures: Surface plasmons, bulk plasmons, and the electron-energy-loss spectrum. *Phys. Rev. B* **29**, 1695 (1984).

18. Camley, R. E. & Mills, D. L. Erratum: Collective excitations of semi-infinite superlattice structures: Surface plasmons, bulk plasmons, and the electron-energy-loss spectrum (Physical Review B (1988) 37, 17, (10378)). *Physical Review B* vol. 37 10378 (1988).

19. Raj, N. & Tilley, D. R. Polariton and effective-medium theory of magnetic

superlattices. *Phys. Rev. B* **36**, 7003–7007 (1987).

20. Giuliani, G. F. & Quinn, J. J. Charge-density excitations at the surface of a semiconductor superlattice: A new type of surface polariton. *Phys. Rev. Lett.* **51**, 919–922 (1983).

21. Deng, H., Haug, H. & Yamamoto, Y. Exciton-polariton Bose-Einstein condensation. *Rev. Mod. Phys.* **82**, 1489–1537 (2010).

22. Kasprzak, J. *et al.* Bose-Einstein condensation of exciton polaritons. *Nature* **443**, 409–414 (2006).

23. Balili, R., Hartwell, V., Snoke, D., Pfeiffer, L. & West, K. Bose-Einstein Condensation of Microcavity Polaritons in a Trap. *Science (80-.).* **316**, 1007–1010 (2007).

24. Ballarini, D. *et al.* All-optical polariton transistor. *Nat. Commun.* **4**, 1778 (2013).

25. Savvidis, P. G. *et al.* Angle-resonant stimulated polariton amplifier. *Phys. Rev. Lett.* **84**, 1547–1550 (2000).

26. Ciuti, C., Schwendimann, P., Deveaud, B. & Quattropani, A. Theory of the angle-resonant polariton amplifier. *Phys. Rev. B* **62**, R4825 (2000).

27. Boventer, I. *et al.* Control of the coupling strength and linewidth of a cavity magnon-polariton. *Phys. Rev. Res.* **2**, 13154 (2020).

28. Ribeiro, R. F., Martínez-Martínez, L. A., Du, M., Campos-Gonzalez-Angulo, J. & Yuen-Zhou, J. Polariton chemistry: controlling molecular dynamics with optical cavities. *Chem. Sci.* **9**, 6325–6339 (2018).

29. Li, X., Mandal, A. & Huo, P. Cavity frequency-dependent theory for vibrational polariton chemistry. *Nat. Commun.* **12**, 1–9 (2021).

30. Klembt, S. *et al.* Exciton-polariton topological insulator. *Nature* **562**, 552–556 (2018).

31. Chen, S. *et al.* Real-space nanoimaging of THz polaritons in the topological insulator Bi2Se3. *Nat. Commun.* **13**, 1–9 (2022).

32. Shang, Q. *et al.* Role of the Exciton-Polariton in a Continuous-Wave Optically Pumped CsPbBr3Perovskite Laser. *Nano Lett.* **20**, 6636–6643 (2020).

33. Kartashov, Y. V & Skryabin, D. V. Two-Dimensional Topological Polariton Laser. *Phys. Rev. Lett.* **122**, 083902 (2019).

34. Kavokin, A. *et al.* Polariton condensates for classical and quantum computing. *Nat. Rev. Phys.* 1–17 (2022) doi:10.1038/s42254-022-00447-1.

35. Macêdo, R. The 2021 magnetic hyperbolic polaritons roadmap. in *Solid State Physics - Advances in Research and Applications* 1–9 (Elsevier Inc., 2021). doi:10.1016/bs.ssp.2021.08.004.

36. Macêdo, R. & Camley, R. E. Engineering terahertz surface magnon-polaritons in hyperbolic antiferromagnets. *Phys. Rev. B* **99**, 014437 (2019).

37. Macêdo, R., Dumelow, T. & Stamps, R. L. Tunable Focusing in Natural Hyperbolic Magnetic Media. *ACS Photonics* **3**, 1670–1677 (2016).

38. Alfaro-Mozaz, F. J. *et al.* Nanoimaging of resonating hyperbolic polaritons in linear boron nitride antennas. *Nat. Commun.* **8**, 1–8 (2017).

39. Yoxall, E. *et al.* Direct observation of ultraslow hyperbolic polariton propagation with negative phase velocity. *Nat. Photonics* **9**, 674–678 (2015).

40. Macêdo, R. & Stamps, R. L. Electromagnetic Waves in Canted Magnets. in *Compendium on Electromagnetic Analysis From Electrostatics to Photonics:*

Fundamentals and Applications for Physicists and Engineers. (ed. Donahue, M.) 231–261 (World Scientific, 2020). doi:10.1142/9789813270268_0007.

41. Macêdo, R., Livesey, K. L. & Camley, R. E. Using magnetic hyperbolic metamaterials as high frequency tunable filters. *Appl. Phys. Lett.* **113**, 121104 (2018).

42. Smith, D. R., Padilla, W. J., Vier, D. C., Nemat-Nasser, S. C. & Schultz, S. Composite medium with simultaneously negative permeability and permittivity. *Phys. Rev. Lett.* **84**, 4184 (2000).

43. Macêdo, R. Tunable Hyperbolic Media: Magnon-Polaritons in Canted Antiferromagnets. in *Solid State Physics - Advances in Research and Applications* vol. 72 93–157 (Academic Press Inc., 2021).

44. Wu, X., McEleney, C. A., González-Jiménez, M. & Macêdo, R. Emergent asymmetries and enhancement in the absorption of natural hyperbolic crystals. *Optica* **6**, 1478 (2019).

45. Macêdo, R., Dumelow, T., Camley, R. E. & Stamps, R. L. Oriented Asymmetric Wave Propagation and Refraction Bending in Hyperbolic Media. *ACS Photonics* **5**, 5086–5094 (2018).

46. Wang, X. *et al.* Extreme Asymmetry in Metasurfaces via Evanescent Fields Engineering: Angular-Asymmetric Absorption. *Phys. Rev. Lett.* **121**, 256802 (2018).

47. Dumelow, T., Da Costa, J. A. P. & Freire, V. N. Slab lenses from simple anisotropic media. *Phys. Rev. B* **72**, 235115 (2005).

48. Estevâm da Silva, R. *et al.* Far-infrared slab lensing and subwavelength imaging in crystal quartz. *Phys. Rev. B* **86**, 155152 (2012).

49. Liu, Y., Bartal, G. & Zhang, X. All-angle negative refraction and imaging in a bulk

medium made of metallic nanowires in the visible region. *Opt. Express* **16**, 15439 (2008).

50. Smith, D. R. & Schurig, D. Electromagnetic Wave Propagation in Media with Indefinite Permittivity and Permeability Tensors. *Phys. Rev. Lett.* **90**, 4 (2003).

51. Maxwell, J. C. *A Treatise on Electricity and Magnetism*. vol. 2 (Clarendon Press, 1873).

52. Rodrigues Da Silva, R. *et al.* Using phonon resonances as a route to all-angle negative refraction in the far-infrared region: The case of crystal quartz. *Phys. Rev. Lett.* **105**, 163903 (2010).

53. Macêdo, R. & Dumelow, T. Tunable all-angle negative refraction using antiferromagnets. *Phys. Rev. B* **89**, 035135 (2014).

54. Fahrenfort, J. Attenuated total reflection. A new principle for the production of useful infra-red reflection spectra of organic compounds. *Spectrochim. Acta* **17**, 698–709 (1961).

55. Otto, A. Excitation of nonradiative surface plasma waves in silver by the method of frustrated total reflection. *Zeitschrift für Phys.* **216**, 398–410 (1968).

56. Wallis, R. F., Maradudin, A. A. & Stegeman, G. I. Surface polariton reflection and radiation at end faces. *Appl. Phys. Lett.* **42**, 764 (1983).

57. Homola, J. Present and future of surface plasmon resonance biosensors. *Analytical and Bioanalytical Chemistry* vol. 377 528–539 (2003).

58. Camley, R. E. *et al.* High-frequency signal processing using magnetic layered structures. *J. Magn. Magn. Mater.* **321**, 2048–2054 (2009).

59. Peng, J. *et al.* Twist-Induced Near-Field Thermal Switch Using Nonreciprocal Surface Magnon-Polaritons. *ACS Photonics* **8**, 2183–2189 (2021).

60. Liu, R. *et al.* Near-field radiative heat transfer in hyperbolic materials. *International Journal of Extreme Manufacturing* vol. 4 032002 (2022).

61. Halevi, P. & Ramos-Mendieta, F. Tunable photonic crystals with semiconducting constituents. *Phys. Rev. Lett.* **85**, 1875 (2000).

62. McCall, S. L. & Hahn, E. L. Self-Induced Transparency. *Phys. Rev.* **183**, 457 (1969).

63. Cho, Y. & Kumamaru, T. Photothermal dielectric spectroscopic microscope. *Rev. Sci. Instrum.* **67**, 19 (1996).

64. Sun, Y., Liu, X.-F., Wang, T.-J. & Gao, Y.-P. Photothermally Induced Transparency in Mode-Cascaded Microcavity. *Adv. Photonics Res.* **1**, 2000016 (2020).

65. Pawlik, G., Tarnowski, K., Walasik, W., Mitus, A. C. & Khoo, I. C. Liquid crystal hyperbolic metamaterial for wide-angle negative–positive refraction and reflection. *Opt. Lett.* **39**, 1744 (2014).

66. Melnyk, O. *et al.* Fast Switching Dual-Frequency Nematic Liquid Crystal Tunable Filters. *ACS Photonics* **8**, 1222–1231 (2021).

67. Wu, X., McEleney, C. A., Shi, Z., González-Jiménez, M. & Macêdo, R. Asymmetric Reflection Induced in Reciprocal Hyperbolic Materials. *ACS Photonics* **9**, 2774–2782 (2022).

68. Gervais, F. & Piriou, B. Temperature dependence of transverse and longitudinal optic modes in the α and β phases of quartz. *Phys. Rev. B* **11**, 3944–3950 (1975).

69. Duarte, J. L., Sanjurjo, J. A. & Katiyar, R. S. Off-normal infrared reflectivity in

uniaxial crystals: α-LiIO3 and α-quartz. *Phys. Rev. B* **36**, 3368 (1987).

70. Sayem, A. Al, Mahdy, M. R. C. & Rahman, M. S. Broad angle negative refraction in lossless all dielectric or semiconductor based asymmetric anisotropic metamaterial. *J. Opt.* **18**, 015101 (2015).

71. Jackson, J. D. *Classical Electrodynamics*. (John Wiley & Sons, 1975).

72. El-Gohary, A. R. *et al.* Observation of surface phonon-polaritons on a MQW specimen by attenuated-total-reflection spectroscopy. *Semicond. Sci. Technol.* **4**, 388–392 (1989).

73. Camley, R. E. Nonreciprocal surface waves. *Surf. Sci. Rep.* **7**, 103–187 (1987).

74. Zangwill, A. *Modern Electrodynamics*. *Modern Electrodynamics* (Cambridge University Press, 2012). doi:10.1017/cbo9781139034777.

75. Kong, J. A., Wu, B.-I. & Zhang, Y. Lateral displacement of a Gaussian beam reflected from a grounded slab with negative permittivity and permeability. *Appl. Phys. Lett* **80**, 2084 (2002).

76. Macêdo, R., Rodrigues da Silva, R., Dumelow, T. & da Costa, J. A. P. MgF2 as a material exhibiting all-angle negative refraction and subwavelength imaging due to the phonon response in the far infrared. *Opt. Commun.* **310**, 94–99 (2014).

77. Stickler, B. A. & Schachinger, E. *Basic concepts in computational physics*. *Basic Concepts in Computational Physics: Second Edition* (Springer, 2016). doi:10.1007/978-3-319-27265-8.

78. Poynting, J. H. XV. On the transfer of energy in the electromagnetic field. *Philos. Trans. R. Soc. London* **175**, 343–361 (1884).

79. Wait, J. R. *Electromagnetic waves in stratified media*. (Pergamon Press, 1970).